IEEE Access
Multidisciplinary | Rapid Review | Open Access Journal

Received 23 September 2023, accepted 16 October 2023, date of publication 23 October 2023, date of current version 1 November 2023.

Digital Object Identifier 10.1109/ACCESS.2023.3327062

RESEARCH ARTICLE

State of Temperature Estimation of Li-Ion Batteries Using 3rd Order Smooth Variable Structure Filter

FARZANEH EBRAHIMI, RYAN AHMED, AND SAEID HABIBI, (Member, IEEE)
Centre for Mechatronics and Hybrid Technologies (CMHT), Department of Mechanical Engineering, McMaster University, Hamilton, ON L8S 4L8, Canada

Corresponding author: Farzaneh Ebrahimi (ebrahf5@mcmaster.ca)

This work was supported by the Ontario Research Fund Research Excellence and Federal Economic Development Agency for Southern Ontario under Grant 08-044 (ORF) and Grant 814996 (FedDev).

ABSTRACT The Battery Management System plays a critical role in ensuring the longevity, safety, and optimal performance of batteries by performing state of charge and health estimation, thermal management, cell balancing, and charge control. Thermal management is a crucial component that is responsible for temperature monitoring and control, managing heat generation and dissipation, preventing thermal runaway, and optimizing battery performance. This paper includes several original contributions. (1) A four-state lumped thermal model is introduced to model the core and surface temperatures of the battery. (2) Accordingly, various characterization tests were conducted on a lithium-ion Prismatic battery to log the thermal behavior of the battery. The third-order Equivalent Circuit Model is used to calculate the generated heat inside the cell using the measured physical parameters such as voltage, and current. (3) Machine learning methods like Particle Swarm Optimization and Genetic Algorithm are used and compared to determine the parameters of the thermal model. (4) A novel, reliable 3rd order Smooth Variable Structure Filter is suggested in this work and evaluated against the Extended Kalman Filter, SVSF, and 2nd-order SVSF. The proposed strategy demonstrated higher accuracy compared to the abovementioned filters.

INDEX TERMS Electric vehicles, Li-Ion batteries, smooth variable structure filter, state estimation, state of temperature (SOT), thermal management.

I. INTRODUCTION

The automotive industry is undergoing a paradigm shift from conventional, human-driven internal combustion engine (ICE)-powered vehicles to battery electric vehicles (BEVs). BEVs offer several advantages over their conventional ICE-powered counterparts since they are more sustainable, greener, cleaner, and require less maintenance. Moreover, BEVs can be powered by renewable sources, such as solar and wind, producing fewer greenhouse gas emissions than their gasoline and diesel counterparts. Battery Packs represent the most expensive component in BEVs, therefore requiring accurate real-time monitoring and control.

A Battery Management System (BMS) is responsible for monitoring and controlling battery cells, preventing any potential dangers, and ensuring their longevity. The BMS performs key critical tasks, such as monitoring battery states, communicating with other onboard systems, cell balancing, and thermal management. The efficiency of the BMS is heavily dependent on the accuracy of the battery model and estimation strategy, as state variables, such as the State of Charge (SOC), State of Health (SOH), State of Power (SOP), and State of Temperature (SOT), cannot be directly measured. The estimation strategy must be robust and adaptable to changes in operating conditions, power demands, temperature, and degradation. However, measurement noise and other factors can affect estimation accuracy in real-time [1].

Battery state estimation has been a topic of extensive research in recent years, mainly focusing on SOC estimation. This estimation can be challenging due to aging, self-discharge, and temperature, which significantly affect the battery performance. It is vital to measure the battery

The associate editor coordinating the review of this manuscript and approving it for publication was Min Wang.

temperature to accurately estimate the battery SOC and SOP and improve battery performance. Moreover, temperature monitoring prevents unnecessary aging of the battery and battery pack failures caused by thermal runaway. Although temperature sensors are frequently used in battery packs, using a sensor for each cell and different parts of the battery is impractical and complicated. Therefore, robust temperature estimation models can be used instead of physical sensors to reduce the number of sensors required and the cost [2].

Several methods have been introduced in the literature for estimating the battery temperature, including electrochemical impedance spectroscopy (EIS), data-driven approaches, and state-space models. EIS is a method used to link the measured impedance of the battery with the temperature. This method requires special BMS hardware for high- and low-frequency measurements and is not feasible for implementation on battery packs during operation [3], [4]. Authors in [5] proposed a method to link EIS and surface temperature to the core temperature using a radial 1-D model at a single frequency. Data-driven strategies leverage artificial intelligence and machine learning algorithms to estimate the SOC and SOT of a battery. These models, despite their accuracy, require a high volume of training data and time [2]. State-space models are the other standard methods that can capture the thermal behavior of batteries with reasonable accuracy. Thermal models use thermal capacitors and resistors to model the heat generation, heat accumulation, and heat dissipation of the battery, considering the thermal boundary conditions. Extensive research has been conducted on the thermal modeling of batteries. Thermal models can be classified into control-oriented and design-oriented models, depending on the application. Control-oriented models are simplified models that try to find a balance between fidelity and computational complexity, while design-oriented models are usually two or 3D models that are mostly focused on fidelity and used offline. A study is done in [6] to compare seven different control-oriented thermal models named lumped-mass, thermal equivalent circuit (TEC), improved TEC (ITEC), polynomial approximation (PA), quadratic assumption (QA), Chebyshev-Galerkin (CG), and finite difference model (FDM), in terms of fidelity, elapsed time, and sensitivity of the models to the convective heat transfer coefficient. Also, thermal models can be divided into electro-thermal models and electrochemical thermal models [7]. The authors of [8] proposed a control-oriented electrothermal model for pouch cells using CG approximation. Two lumped mass submodels for the tabs and a 2-D CG submodel for the body compose the entire model, which is parameterized by Particle Swarm Optimization (PSO) using different drive cycles over a wide temperature range. Also, a 3D body and post submodels for a pouch cell are used [9]. A neural network algorithm is used to find the relationship among battery resistance, temperature, SOC, and the rate of discharge. Authors in [10] studied the core and surface temperatures by measuring them using embedded thermocouples under forced convection conditions. This research also provides practical measures for measuring core temperature. Specific heat capacity is one of the crucial parameters of the thermal model in which a calorimeter is required to determine it, but a method was proposed in [11] to calculate it for different Li-ion batteries regardless of their shapes. The thermal model of a Prismatic battery was studied by comparing its thermophysical properties at various operating temperatures. The obtained heat capacity and thermal conductivity values were used in the lumped and 3D thermal models. The results show that while the heat capacity can be slightly affected by temperature changes, the thermal conductivity will remain the same for every temperature [12]. The relationship between the battery voltage and thermal models was studied using three sub-models: the electrochemical, heat generation, and thermal models. The battery was tested under isothermal and non-isothermal operating conditions to determine the model parameters. One of the innovations of this research is to define three different surface states instead of one that makes the thermal model computationally more complicated but enables BMS to have a better estimation of the surface temperature [13].

Filters and observers are widely used methods for obtaining states that are not measurable directly or are costly to measure. Having access to an accurate model and stochastic properties of the system are the basic preliminaries that help us benefit from the advantages of the estimators and observers. By using different estimation algorithms and measurable variables such as the current and voltage, the SOT or other states can be easily estimated [1]. Authors in [14] proposed an adaptive Potter filter to estimate the core temperature by using a lumped thermal model. This closed-loop estimation strategy estimates the surface and core temperatures even under high-current pulses and model uncertainties. Another adaptive observer is used on the lumped thermal model, which is derived using the recursive least-squares method for online parameter identification. This study also used the forgetting factor to estimate the internal resistance and SOH of the battery [15]. A sliding mode observer is used in [16] to estimate the disturbed temperature of a pouch cell using a 2D thermal model. This study mainly focuses on determining the minimum number of required sensors and their effective locations.

Kalman filter (KF) is a powerful estimation strategy that is used in [17] to estimate the SOT of the battery to mitigate the model uncertainties. This study used a more accurate heat generation model by considering the effects of changes in entropy and overpotential on heat generation. An interval observer is used on battery packs to estimate the SOC and the temperature of the cells, and the difference between the proposed observer and Extended Kalman Filter (EKF)in terms of computational costs shows its superiority [18]. Moreover, EKF is used on a novel simplified thermoelectric model, which includes a simplified thermal model interrelated to the electric model, to estimate the core temperature [19]. Authors in [20] focused on sensorless temperature estimation based

on the impedance and used EKF on an EIS- thermal combined model. In addition, in this study, in order to estimate the convection coefficient at the cell surface, a dual EKF is introduced. Dual EKF is also used in [21] to estimate the SOC a SOH by using the electrical model of the battery, then a physics-based reduced-order thermal model is introduced to estimate the core and surface temperature by just using the ambient temperature and the generated heat. It is shown that having an accurate battery model and updating the electrical parameters affects the sensorless temperature estimation of the battery over the lifetime of the battery.

Estimation strategies, particularly Kalman-based filters, have been broadly used to estimate battery states. The Smooth Variable Structure Filter (SVSF) is a model-based robust filter. This filter takes advantage of an inherent switching action to maintain the estimation error within an acceptable region [22]. In [23], SVSF was used to estimate the SOC. Furthermore, the SOH is obtained using the chattering signal in six different battery models. Genetic Algorithm (GA) [24], as an offline in addition to a Recursive Square Root (RLS) [25] as an online parameter identification method were used, and then SVSF was applied for the SOC estimation of the new and aged batteries. In another study, SVSF was used to estimate the SOC, but the main contribution in comparison to other studies is that they used the weighted EKF for parameter identification. In addition, they included SOH estimation by estimating the maximum capacitance [26]. In [27], a new estimation strategy is applied, which is a combination of the Interacting Multiple Model (IMM) with SVSF and a variable boundary layer (VBL). In this study, multiple models for different states of life were used to estimate the SOC and internal resistance. These estimates, along with the mode probability from the IMM outlining the most applicable model, were used to estimate SOH and SOP. Additionally, in this study, Coulomb counting is considered as an additional measurement to improve the estimation accuracy. The same approach has been applied to 3rd order Equivalent Circuit Model (ECM)to estimate the SOC at low temperatures [28]. EKF-SVSF is a well-known approach that uses a switching strategy between the EKF and SVSF based on a variable boundary layer. The authors in [29] used this filter to estimate the SOC and to demonstrate the superiority of the method compared to the EKF and SVSF. The 2nd-order SVSF is another SVSF-based filter that eliminates chattering problems by introducing a new filter gain. This filter is more complicated than SVSF since it uses a square root function [30]. Introducing a new definition for the backward difference operator leads to a new gain that uses more information and is more accurate than the other SVSF-based filters. Although SVSF based filters are widely used to estimate SOC and SOH, they have not been used in thermal models to estimate SOT. This study introduces a new SVSF based filter based on 3rd derivate of the error. The stability of the proposed filter is proven using a Lyapunov function. The new method also improves the robustness of the SVSF based filters, while slightly increasing the computational complexity in compared to 2nd order SVSF. The results also indicate that the gain of the new filter can mitigate the chattering effect of the SVSF, resulting in better estimation.

The remainder of this paper is organized as follows. Section II lays the foundation for the 3rd order SVSF algorithm and its stability proof. Section III presents the thermal model of the battery, the experimental setup, and parameter identification. Section IV covers the performance of the different filters in estimating the battery temperatures in terms of accuracy and computational complexity. Finally, the conclusions, results, and future work are presented.

II. FILTER DEVELOPMENT

This section covers the development of a novel robust state estimation method. Third-order SVSF is a model-based filter that satisfies the sliding conditions [30]. The proposed filter is different from the traditional SVSF in terms of gain and boundary layers, as it not only maintains precision and robustness but also effectively eliminates chattering problems. Third-order SVSF benefits the accuracy of the third-order delta definition (Sterling interpolation formula) by using more information compared to other SVSF-based filters. This filter is designed for nonlinear plants and can operate without full measurements. For states without associated measurements, Luenberger's transformation is used to decrease the estimation error [18].

A. PROBLEM FORMULATION

The nonlinear discrete-time system considered can be described as

$$\boldsymbol{x}_{k+1} = f(\boldsymbol{x}_k, \boldsymbol{u}_k, \boldsymbol{\omega}_k) \tag{1}$$

$$\boldsymbol{z}_k = H\boldsymbol{x}_k + \boldsymbol{v}_k \tag{2}$$

where $\boldsymbol{x}_k \in R^n$ and $z_k \in R^m$ are respectively the state and the measurement vector at epoch k; f (.) is the nonlinear process function, H is the measurement matrix. $\boldsymbol{\omega}_k$ and $\boldsymbol{v}_k$ represent the process and measurement noise with zero means, and $\boldsymbol{u}_k$ is known as control vector. Systems with modeled as (1) and (2) are assumed to be smooth with continuous partial derivatives. Using these assumptions, the algorithm for 3rd order SVSF is considered as follows:

1) PREDICTION STAGE

1. The a priori state estimate vector

$$\widehat{\boldsymbol{x}}_{k+1|k} = f(\widehat{\boldsymbol{x}}_k, \boldsymbol{u}_k) \tag{3}$$

$$\widehat{\boldsymbol{z}}_{k+1|k} = H\widehat{x}_{k+1|k} \tag{4}$$

2. The a posteriori measurement error and a priori measurement error vector

$$\boldsymbol{e}_{z_{k|k}} = \boldsymbol{z}_k - H\widehat{\boldsymbol{x}}_{k|k} \tag{5}$$

$$\boldsymbol{e}_{z_{k+1|k}} = \boldsymbol{z}_{k+1} - H\widehat{\boldsymbol{x}}_{k+1|k} \tag{6}$$

2) UPDATE STAGE

3. Corrective gain

$$\boldsymbol{K}_{k+1} = H^{-1}\Bigg[\boldsymbol{e}_{z_{k+1|k}} - \boldsymbol{e}_{z_{k|k}} + \frac{\boldsymbol{e}_{z_{k-1|k-1}}}{2} - sqrt\Bigg(\frac{\left(\boldsymbol{e}_{z_{k-1|k-1}} \circ \boldsymbol{e}_{z_{k-1|k-1}}\right)}{4} - \left(\boldsymbol{e}_{z_{k|k}} \circ \boldsymbol{e}_{z_{k|k}}\right) + \left(\boldsymbol{e}_{z_{k-1|k-1}} \circ \boldsymbol{e}_{z_{k|k}}\right) + \frac{\gamma^2\left(\boldsymbol{E}_{z_{k|k}} \circ \boldsymbol{E}_{z_{k|k}}\right)}{2}\Bigg)\Bigg] \quad (7)$$

4. a posteriori estimates

$$\widehat{\boldsymbol{x}}_{k+1|k+1} = \widehat{\boldsymbol{x}}_{k+1|k} + \boldsymbol{K}_{k+1} \quad (8)$$

Remark: H^{-1} represents the pseudo-invers of the H matrix where $m \neq n$. Also, initially it is assumed that H is full rank meaning that all the states are measurable. Then, the corrective gain for the cases without full state measurement is also discussed.

B. THIRD-ORDER SVSF FOR CASES WITH FULL STATE MEASUREMENT ($m = n$)

Definition: With new definition for backward difference operator as below (the idea originated from the Stirling formula [31]):

$$\boldsymbol{E}_{z_{k|k}} = \boldsymbol{e}_{z_{k|k}} + \boldsymbol{e}_{z_{k-2|k-2}} - 2\boldsymbol{e}_{z_{k-1|k-1}} \quad (9)$$

Theorem: The proposed filter with a constant coefficient $\gamma(0 < \gamma < 1)$ is stable and the state estimates will converge to a neighborhood of the true state trajectory.

Proof: With a new Lyapunov function candidate as:

$$V_k = \left(\boldsymbol{e}_{z_{k-1|k-1}} \circ \boldsymbol{e}_{z_{k-1|k-1}}\right) + \left(\boldsymbol{e}_{z_{k|k}} \circ \boldsymbol{e}_{z_{k|k}}\right) + \left(\boldsymbol{E}_{z_{k|k}} \circ \boldsymbol{E}_{z_{k|k}}\right) \quad (10)$$

The symbol $(\circ)$ represents the Shur product. Based on Lyapunov's theory, the system is stable if $\Delta V_{k+1} = V_{k+1} - V_k < 0$ [2].

Equation (7) can be rearranged as below:

$$\boldsymbol{e}_{z_{k+1|k}} - H\boldsymbol{K}_{k+1} = \boldsymbol{e}_{z_{k|k}} - \frac{\boldsymbol{e}_{z_{k-1|k-1}}}{2} + sqrt\Bigg(\frac{\left(\boldsymbol{e}_{z_{k-1|k-1}} \circ \boldsymbol{e}_{z_{k-1|k-1}}\right)}{4} - \left(\boldsymbol{e}_{z_{k|k}} \circ \boldsymbol{e}_{z_{k|k}}\right)\left(\boldsymbol{e}_{z_{k-1|k-1}} \circ \boldsymbol{e}_{z_{k|k}}\right) + \frac{\gamma^2\left(\boldsymbol{E}_{z_{k|k}} \circ \boldsymbol{E}_{z_{k|k}}\right)}{2}\Bigg) \quad (11)$$

By using (8), we have:

$$\boldsymbol{e}_{z_{k+1|k}} - H(\widehat{x}_{k+1|k+1} - \widehat{x}_{k+1|k}) = \boldsymbol{e}_{z_{k|k}} - \frac{\boldsymbol{e}_{z_{k-1|k-1}}}{2} + sqrt\Bigg(\frac{\left(\boldsymbol{e}_{z_{k-1|k-1}} \circ \boldsymbol{e}_{z_{k-1|k-1}}\right)}{4} - \left(\boldsymbol{e}_{z_{k|k}} \circ \boldsymbol{e}_{z_{k|k}}\right)\left(\boldsymbol{e}_{z_{k-1|k-1}} \circ \boldsymbol{e}_{z_{k|k}}\right) + \frac{\gamma^2\left(\boldsymbol{E}_{z_{k|k}} \circ \boldsymbol{E}_{z_{k|k}}\right)}{2}\Bigg) \quad (12)$$

Equations (5) and (6) yields to $\boldsymbol{e}_{z_{k+1|k+1}} - \boldsymbol{e}_{z_{k+1|k}} = -H(\widehat{\boldsymbol{x}}_{k+1|k+1} - \widehat{\boldsymbol{x}}_{k+1|k})$; therefore, by rearranging (12), we have:

$$\left(\boldsymbol{e}_{z_{k+1|k+1}} - \boldsymbol{e}_{z_{k|k}} + \frac{\boldsymbol{e}_{z_{k-1|k-1}}}{2}\right) \circ \left(\boldsymbol{e}_{z_{k+1|k+1}} - \boldsymbol{e}_{z_{k|k}} + \frac{\boldsymbol{e}_{z_{k-1|k-1}}}{2}\right) - \frac{\left(\boldsymbol{e}_{z_{k-1|k-1}} \circ \boldsymbol{e}_{z_{k-1|k-1}}\right)}{4} + \left(\boldsymbol{e}_{z_{k|k}} \circ \boldsymbol{e}_{z_{k|k}}\right) - \left(\boldsymbol{e}_{z_{k-1|k-1}} \circ \boldsymbol{e}_{z_{k|k}}\right) = \frac{\gamma^2\left(\boldsymbol{E}_{z_{k|k}} \circ \boldsymbol{E}_{z_{k|k}}\right)}{2} \quad (13)$$

With $0 < \gamma < 1$, the equality (13) turns into following inequality:

$$2\left(\boldsymbol{e}_{z_{k+1|k+1}} - \boldsymbol{e}_{z_{k|k}} + \frac{\boldsymbol{e}_{z_{k-1|k-1}}}{2}\right) \circ \left(\boldsymbol{e}_{z_{k+1|k+1}} - \boldsymbol{e}_{z_{k|k}} + \frac{\boldsymbol{e}_{z_{k-1|k-1}}}{2}\right) - \frac{\left(\boldsymbol{e}_{z_{k-1|k-1}} \circ \boldsymbol{e}_{z_{k-1|k-1}}\right)}{2} + 2\left(\boldsymbol{e}_{z_{k|k}} \circ \boldsymbol{e}_{z_{k|k}}\right) - 2\left(\boldsymbol{e}_{z_{k-1|k-1}} \circ \boldsymbol{e}_{z_{k|k}}\right) < \left(\boldsymbol{E}_{z_{k|k}} \circ \boldsymbol{E}_{z_{k|k}}\right) \quad (14)$$

Expanding the above inequality leads to:

$$2\left(\boldsymbol{e}_{z_{k+1|k+1}} \circ \boldsymbol{e}_{z_{k+1|k+1}}\right) + 4\left(\boldsymbol{e}_{z_{k|k}} \circ \boldsymbol{e}_{z_{k|k}}\right) - 4\left(\boldsymbol{e}_{z_{k+1|k+1}} \circ \boldsymbol{e}_{z_{k|k}}\right) + 2\left(\boldsymbol{e}_{z_{k+1|k+1}} \circ \boldsymbol{e}_{z_{k-1|k-1}}\right) - 4\left(\boldsymbol{e}_{z_{k-1|k-1}} \circ \boldsymbol{e}_{z_{k|k}}\right) < \left(\boldsymbol{E}_{z_{k|k}} \circ \boldsymbol{E}_{z_{k|k}}\right) \quad (15)$$

Adding $\boldsymbol{e}_{z_{k-1|k-1}} \circ \boldsymbol{e}_{z_{k-1|k-1}}$ to both sides of the inequality and rearranging yield to following relation:

$$\left(\boldsymbol{e}_{z_{k+1|k+1}} \circ \boldsymbol{e}_{z_{k+1|k+1}}\right) + \Big[\left(\boldsymbol{e}_{z_{k+1|k+1}} \circ \boldsymbol{e}_{z_{k+1|k+1}}\right) + \left(\boldsymbol{e}_{z_{k-1|k-1}} \circ \boldsymbol{e}_{z_{k-1|k-1}}\right) + 4\left(\boldsymbol{e}_{z_{k|k}} \circ \boldsymbol{e}_{z_{k|k}}\right) - 4\left(\boldsymbol{e}_{z_{k+1|k+1}} \circ \boldsymbol{e}_{z_{k|k}}\right) + 2\left(\boldsymbol{e}_{z_{k+1|k+1}} \circ \boldsymbol{e}_{z_{k-1|k-1}}\right) - 4\left(\boldsymbol{e}_{z_{k-1|k-1}} \circ \boldsymbol{e}_{z_{k|k}}\right)\Big] < \left(\boldsymbol{e}_{z_{k-1|k-1}} \circ \boldsymbol{e}_{z_{k-1|k-1}}\right) + \left(\boldsymbol{E}_{z_{k|k}} \circ \boldsymbol{E}_{z_{k|k}}\right) \quad (16)$$

Again, with adding $\boldsymbol{e}_{z_{k|k}} \circ \boldsymbol{e}_{z_{k|k}}$ to both sides we have:

$$\boldsymbol{e}_{z_{k+1|k+1}} \circ \boldsymbol{e}_{z_{k+1|k+1}} + \boldsymbol{e}_{z_{k|k}} \circ \boldsymbol{e}_{z_{k|k}} + \left(\boldsymbol{e}_{z_{k+1|k+1}} + \boldsymbol{e}_{z_{k-1|k-1}} - 2\boldsymbol{e}_{z_{k|k}}\right) \circ \left(\boldsymbol{e}_{z_{k+1|k+1}} + \boldsymbol{e}_{z_{k-1|k-1}} - 2\boldsymbol{e}_{z_{k|k}}\right) < \boldsymbol{e}_{z_{k|k}} \circ \boldsymbol{e}_{z_{k|k}} + \boldsymbol{e}_{z_{k-1|k-1}} \circ \boldsymbol{e}_{z_{k-1|k-1}} + \boldsymbol{E}_{z_{k|k}} \circ \boldsymbol{E}_{z_{k|k}} \quad (17)$$

With the definition given in (9) and (10) we arrive at the following relation which satisfies the stability of the proposed algorithm.

$$V_{k+1} < V_k \quad (18)$$

The proposed approach is more accurate than 2nd order SVSF due to having access to more initial error information. In other words, 3rd order SVSF needs an additional a posteriori measurement error, in backward difference operator

equation (9). It will be shown that this will improve the performance of the 3rd order SVSF at a cost of slightly increased computational cost.

C. THIRD-ORDER SVSF FOR CASES WITHOUT FULL STATE MEASUREMENT ($m \neq n$)

Full state measurement systems have measurements associated with each state. In practical systems this condition is uncommon and costly. Therefore, for controllable and observable systems, the measurement matrix can be decomposed into two parts as: $H = \begin{bmatrix} H_1 & H_2 \end{bmatrix}$, which H_1 is of rank m and H_2 a null matrix. The measurement vector can be written as follows by using Luenberger's transformation:

$$T\boldsymbol{x}_k = \begin{bmatrix} \boldsymbol{z} \\ \boldsymbol{y}_l \end{bmatrix} \tag{19}$$

where T is a transformation matrix, $\boldsymbol{z} \in R^{m\times 1}$ are the measurements associated with the states and $\boldsymbol{y_l} \in R^{(n-m)\times 1}$ are the artificial states. Similar to [22], predicted and updated measurement error for the artificial vector, $\boldsymbol{y}_l$, can be written:

$$\boldsymbol{e}_{y_{l,k|k}} = \Phi_{12}^{-1}\boldsymbol{e}_{z_{k+1|k}} \tag{20}$$

$$\boldsymbol{e}_{y_{l,k+1|k}} = \Phi_{22}\Phi_{12}^{-1}\boldsymbol{e}_{z_{k+1|k}} \tag{21}$$

where $\boldsymbol{e}_{y_l} \in R^{(n-m)\times 1}$ is the artificial measurement error vector. The gain for updating the unmeasured part of the states can be transformed into the following relation by using (20) and (21)

$$\begin{aligned}\boldsymbol{K}_{k+1} = \Bigg[& \Phi_{22}\Phi_{12}^{-1}\boldsymbol{e}_{z_{k+1|k}} - \Phi_{12}^{-1}\boldsymbol{e}_{z_{k+1|k}} + \frac{\Phi_{12}^{-1}\boldsymbol{e}_{z_{k|k-1}}}{2} \\ & -\Phi_{12}^{-1}\,sqrt\left(\frac{\left(\boldsymbol{e}_{z_{k|k-1}} \circ \boldsymbol{e}_{z_{k|k-1}}\right)}{4} - \left(\boldsymbol{e}_{z_{k+1|k}} \circ \boldsymbol{e}_{z_{k+1|k}}\right)\right. \\ & \left. + \left(\boldsymbol{e}_{z_{k|k-1}} \circ \boldsymbol{e}_{z_{k+1|k}}\right) + \frac{\gamma^2\left(\boldsymbol{E}_{z_{k+1|k}} \circ \boldsymbol{E}_{z_{k+1|k}}\right)}{2}\right)\Bigg]\end{aligned} \tag{22}$$

Therefore, the new corrective gain can be rewritten as follows by using (7) for measurable states and (22) for unmeasurable ones:

$$\begin{aligned}&\boldsymbol{K}_{k+1} \\ &= \begin{cases} H^{-1}\begin{bmatrix} \boldsymbol{e}_{z_{k+1|k}} - \boldsymbol{e}_{z_{k|k}} + \frac{\boldsymbol{e}_{z_{k-1|k-1}}}{2} - \\ sqrt\left(\frac{\left(\boldsymbol{e}_{z_{k-1|k-1}} \circ \boldsymbol{e}_{z_{k-1|k-1}}\right)}{4} - \left(\boldsymbol{e}_{z_{k|k}} \circ \boldsymbol{e}_{z_{k|k}}\right)\right. \\ \left. + \left(\boldsymbol{e}_{z_{k-1|k-1}} \circ \boldsymbol{e}_{z_{k|k}}\right) + \frac{\gamma^2\left(\boldsymbol{E}_{z_{k|k}} \circ \boldsymbol{E}_{z_{k|k}}\right)}{2}\right) \end{bmatrix} \\ \begin{bmatrix} \Phi_{22}\Phi_{12}^{-1}\boldsymbol{e}_{z_{k+1|k}} - \Phi_{12}^{-1}\boldsymbol{e}_{z_{k+1|k}} + \frac{\Phi_{12}^{-1}\boldsymbol{e}_{z_{k|k-1}}}{2} - \\ \Phi_{12}^{-1}\,sqrt\left(\frac{\left(\boldsymbol{e}_{z_{k|k-1}} \circ \boldsymbol{e}_{z_{k|k-1}}\right)}{4} - \left(\boldsymbol{e}_{z_{k+1|k}} \circ \boldsymbol{e}_{z_{k+1|k}}\right) + \right. \\ \left. \left(\boldsymbol{e}_{z_{k|k-1}} \circ \boldsymbol{e}_{z_{k+1|k}}\right) + \frac{\gamma^2\left(\boldsymbol{E}_{z_{k+1|k}} \circ \boldsymbol{E}_{z_{k+1|k}}\right)}{2}\right) \end{bmatrix} \end{cases}\end{aligned} \tag{23}$$

Lemma: 3rd order SVSF is stable for the unmeasurable states with the gain introduced in (22).

Proof: Gain in (22) can be rewritten by using (20) and (21) as follows:

$$\begin{aligned}\boldsymbol{K}_{k+1} = & \boldsymbol{e}_{y_{l,k+1|k}} - \boldsymbol{e}_{y_{l,k|k}} + \frac{\boldsymbol{e}_{y_{l,k-1|k-1}}}{2} \\ & - sqrt\left(\frac{\left(\boldsymbol{e}_{y_{l,k-1|k-1}} \circ \boldsymbol{e}_{y_{l,k-1|k-1}}\right)}{4}\right. \\ & - \left(\boldsymbol{e}_{y_{l,k|k}} \circ \boldsymbol{e}_{y_{l,k|k}}\right) + \left(\boldsymbol{e}_{y_{l,k-1|k-1}} \circ \boldsymbol{e}_{y_{l,k|k}}\right) \\ & \left. + \frac{\gamma^2\left(\boldsymbol{E}_{y_{l,k|k}} \circ \boldsymbol{E}_{y_{l,k|k}}\right)}{2}\right)\end{aligned} \tag{24}$$

With Lyapunov function and backward difference operator defined as $V_k = \left(\boldsymbol{e}_{y_{l,k-1|k-1}} \circ \boldsymbol{e}_{y_{l,k-1|k-1}}\right) + \left(\boldsymbol{e}_{y_{l,k|k}} \circ \boldsymbol{e}_{y_{l,k|k}}\right) + \left(\boldsymbol{E}_{y_{l,k|k}} \circ \boldsymbol{E}_{y_{l,k|k}}\right)$ and $\boldsymbol{E}_{y_{l,k|k}} = \boldsymbol{e}_{y_{l,k|k}} + \boldsymbol{e}_{y_{l,k-2|k-2}} - 2\boldsymbol{e}_{y_{l,k-1|k-1}}$ respectively, the stability proof of the 3rd order SVSF for unmeasurable states can be repeated similar to (10)-(18) and lead to $V_{k+1} < V_k$.

III. THERMAL MODEL

Unlike cylindrical batteries that have a uniform geometry, Prismatic batteries' geometry have distinct features. Their unique configuration, coupled with their larger size enable us to differentiate between the various parts of the battery by considering different states for each of them. Therefore, more complicated battery geometry leads us to move from simple models suitable for cylindrical batteries [14] to more complex ones [13]. Consequently, the electrochemical reactions in the cell were neglected and the thermal behavior of the battery is modeled by using four lumped thermal nodes interconnected by thermal resistances and capacitances. Equation (25) represents the thermal model of the battery using four states. As is shown in Fig. 1 three different nodes are considered on battery as tab, housing, and bottom. The tab node is considered as the average temperature of the positive and negative terminals. The housing and bottom nodes represent the heat conduction of the housing and bottom shell of the battery.

$$\begin{aligned} C_t\frac{dT_t}{dt} &= \frac{T_f - T_t}{R_7} + \frac{T_c - T_t}{R_4} + \frac{T_h - T_t}{R_5} \\ C_h\frac{dT_h}{dt} &= \frac{T_b - T_h}{R_2} + \frac{T_c - T_h}{R_1} + \frac{T_t - T_h}{R_5} + \frac{T_f - T_h}{R_8} \\ C_c\frac{dT_c}{dt} &= \dot{s}_r + \frac{T_b - T_c}{R_3} + \frac{T_t - T_c}{R_4} + \frac{T_h - T_c}{R_1} \\ C_b\frac{dT_b}{dt} &= \frac{T_f - T_b}{R_6} + \frac{T_c - T_b}{R_3} + \frac{T_h - T_b}{R_2} \end{aligned} \tag{25}$$

Moreover, a node named as core is considered inside the battery that due to the electrochemical reactions, is assumed to be the source of the generated heat with zero flux at the center. The heat generation rate, $\dot{s}_r$, can be considered as follows:

$$\dot{s}_r = R_0 I^2 \tag{26}$$

where R_0 is the internal resistor of the battery associated with the different temperatures and SOC of the battery. A third

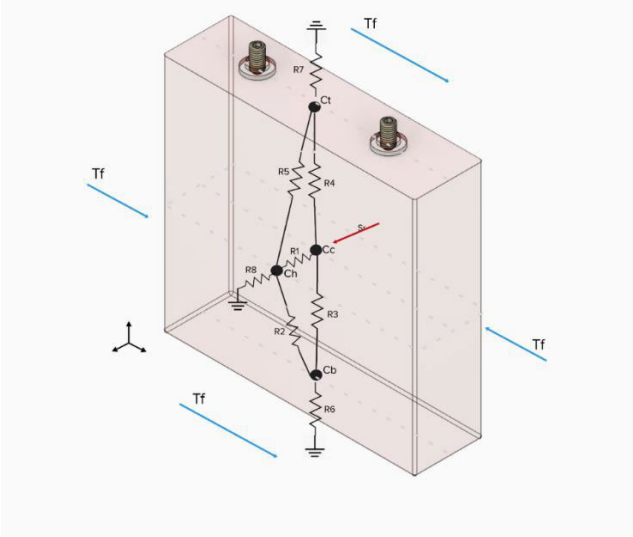

FIGURE 1. A visual representation of the lumped temperature model of a prismatic cell.

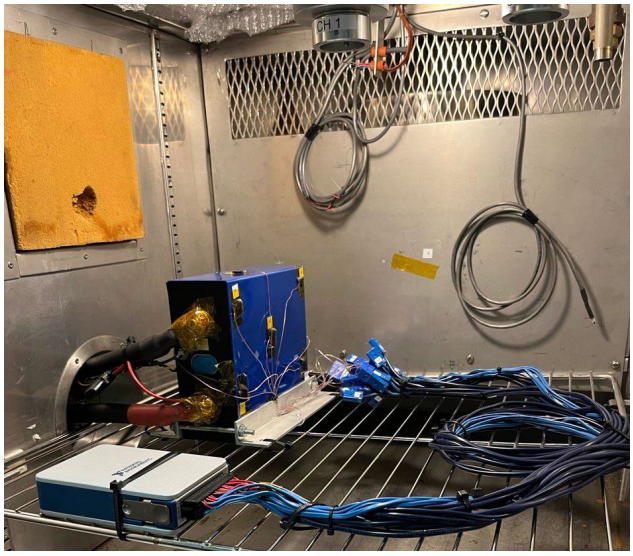

FIGURE 2. Battery setup inside the thermal chamber.

order ECM is used to model the battery and calculate the R_0. Also, R_i, i= 1, . . . , 8 represents the thermal resistors and C_t, C_h, C_c and C_b are the thermal capacitors for tab, housing, core and bottom nodes of the battery. The values for thermal resistors and capacitors can be calculated from battery characterization tests. I is the battery current and T_f is the ambient temperature which is considered as input for this model. The thermal conductance and the heat capacity can be assumed independent of temperature and SOC, therefore (25) can be represented in a discrete time state space form as:

$$\boldsymbol{x}_{k+1} = A\boldsymbol{x}_k + B\boldsymbol{u}_k \tag{27}$$

$$\boldsymbol{z}_k = H\boldsymbol{x}_k + D\boldsymbol{u}_k \tag{28}$$

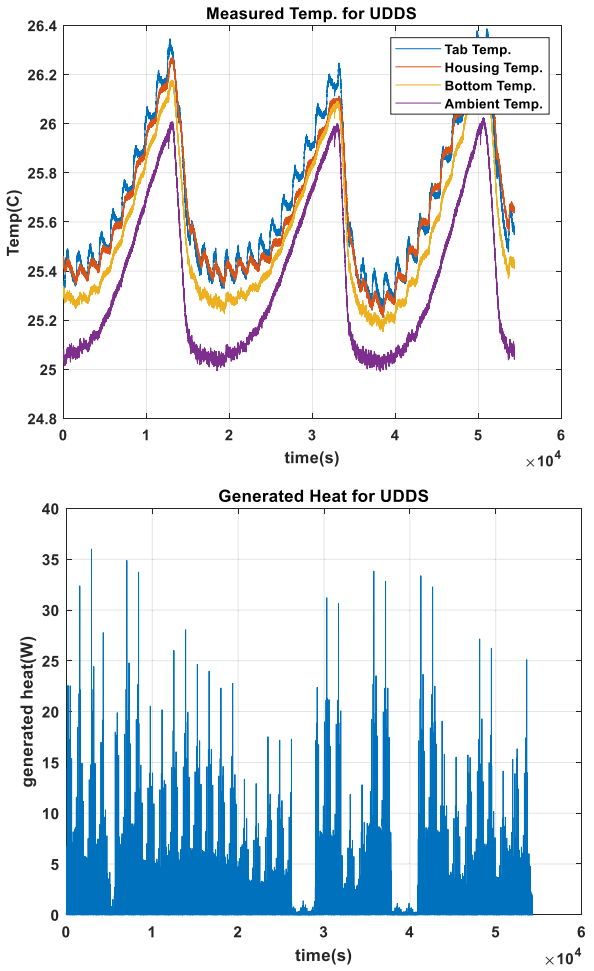

FIGURE 3. Measured temperature and generated heat for the UDDS drive cycle.

where

$$\boldsymbol{x}_k = \begin{bmatrix} T_t \\ T_h \\ T_c \\ T_b \end{bmatrix} \tag{29}$$

$$\boldsymbol{u} = \begin{bmatrix} \dot{s}_r \\ T_f \end{bmatrix} \tag{30}$$

Therefore, considering ΔT as sample time, A and B can be considered as follows (31), as shown at the bottom of the next page.

$$B = \begin{bmatrix} 0 & \frac{\Delta T}{C_t R_7} \\ 0 & \frac{\Delta T}{C_h R_8} \\ \frac{\Delta T}{C_c} & 0 \\ 0 & \frac{\Delta T}{C_b R_6} \end{bmatrix} \tag{32}$$

With the tab measurement as the only measurement, we can consider H = [1 0 0 0] and D= 0.

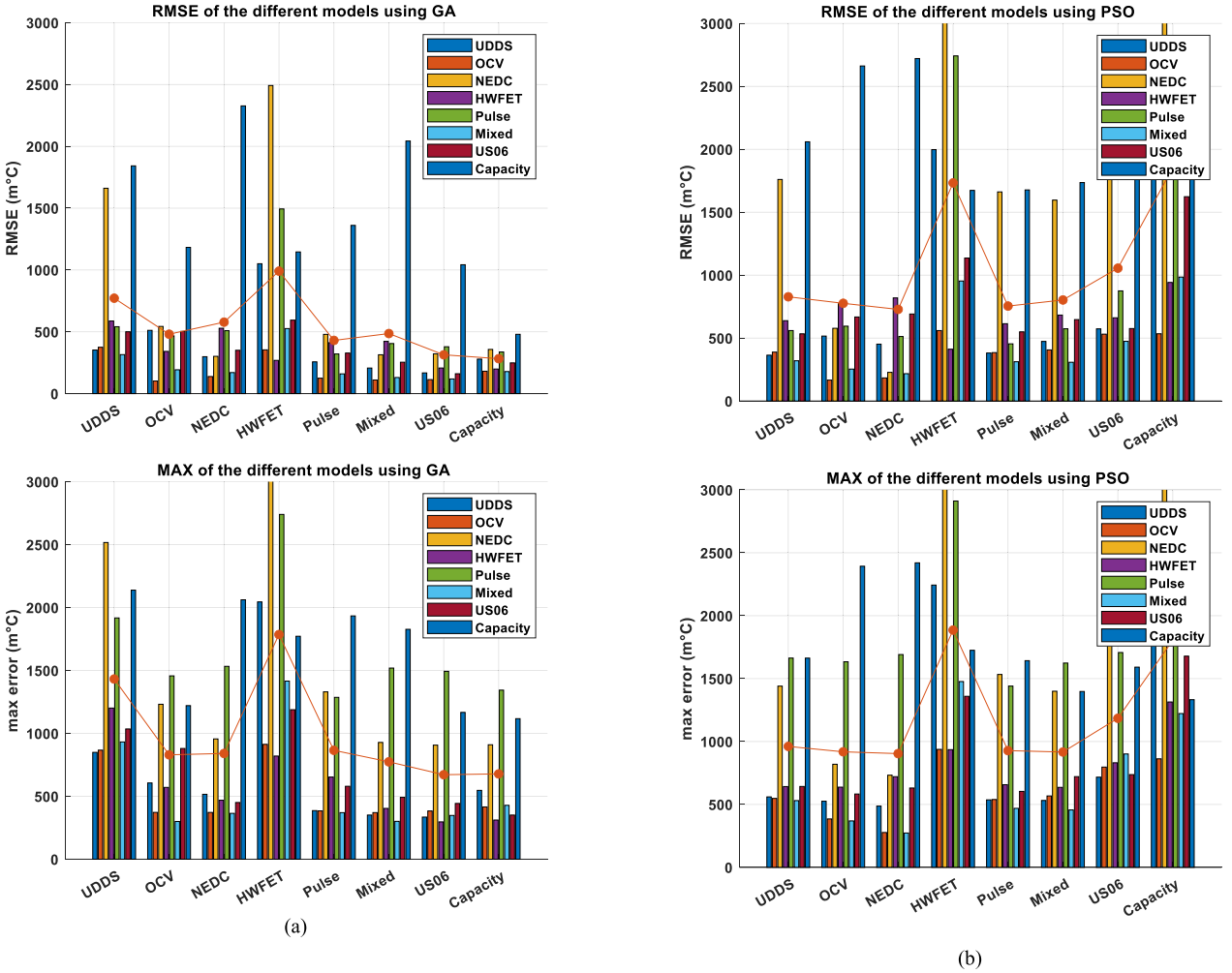

FIGURE 4. RMSE and Max error of the different models (a) using GA (b) using PSO.

A. EXPERIMENTAL SETUP

This paper studies the thermal model of the Prismatic battery LFP 280 (Lithium Iron Phosphate with a C-rate of 280Amps) [32]. To identify the thermal parameters as well as internal resistance of the battery, a series of tests including Open Circuit Voltage (OCV), capacity, pulse discharge, and drive cycle tests including Highway Fuel Economy Test (HWFET), Supplemental Federal Test Procedure (US06), Urban Dynamometer Driving Schedule (UDDS), New European Driving Cycle (NEDC), and Mixed (consisting of the UDDS, HWFET and US06 drive cycles) were designed. The battery was cycled under different current profiles while it was located inside a thermal chamber and was continuously exposed to the chamber air from all six sides as can be seen in Fig. 2. Ten thermocouples were attached to designated points to log the ambient temperature and thermal behavior of the battery under different tests. LabVIEW is used to log thermocouple temperatures by using National Instruments NI-9213 thermocouple module. Due to the safety issues and the fact that inserting a thermocouple inside a battery might change the electrochemical behavior of the battery, the core temperature is not measured.

$$A = \begin{bmatrix} 1-\frac{\Delta T}{C_t}\left(\frac{1}{R_4}+\frac{1}{R_5}+\frac{1}{R_7}\right) & \frac{1}{C_t R_5} & \frac{1}{C_t R_4} & 0 \\ \frac{1}{C_h R_5} & 1-\frac{\Delta T}{C_h}\left(\frac{1}{R_1}+\frac{1}{R_2}+\frac{1}{R_5}+\frac{1}{R_8}\right) & \frac{1}{C_h R_1} & \frac{1}{C_h R_2} \\ \frac{1}{C_c R_4} & \frac{1}{C_c R_1} & 1-\frac{\Delta T}{C_c}\left(\frac{1}{R_1}+\frac{1}{R_3}+\frac{1}{R_4}\right) & \frac{1}{C_c R_3} \\ 0 & \frac{1}{C_b R_2} & \frac{1}{C_b R_3} & 1-\frac{\Delta T}{C_b}\left(\frac{1}{R_2}+\frac{1}{R_3}+\frac{1}{R_6}\right) \end{bmatrix} \quad (31)$$

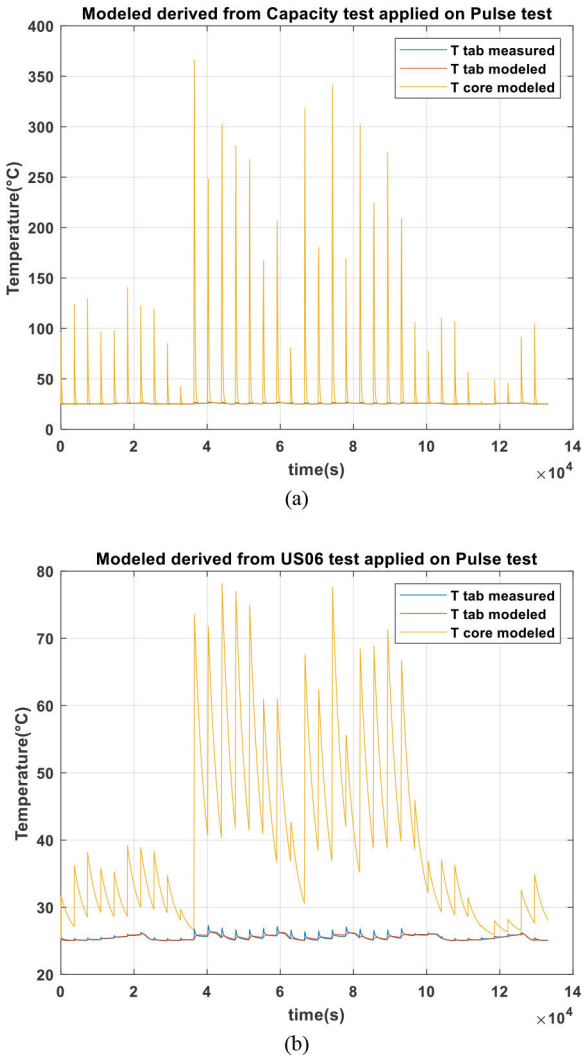

FIGURE 5. Models derived from (a) Capacity test (b) US06 drive cycle test on pulse test.

Fig. 3 shows the logged temperature from different thermocouples and their generated heat for UDDS tests. As it was expected different parts of battery have different thermal behavior.

B. THERMAL MODEL PARAMETRIZATION

The measured battery temperatures from experimental tests are used to obtain the thermal model parameters. Since the model represented in (25) has 12 parameters to be identified, powerful methods are needed to be used. For this purpose, GA and PSO methods have been used for different tests to find suitable values for the parameters. In order to have the best outcome for the parametrization, the population size and the number of generations for GA were considered as 5000 and 50, respectively. Also, a swarm size of 5000 and a max iteration of 50 is considered for PSO. Also, the lower and upper bound was set based on sound physical principles and relevant heat transfer mechanisms. After parametrization, the different outcomes need to be validated. Real test data are used to validate the different models. As it is clear from Fig. 4, GA has better performance in compared to PSO, since it could achieve less RMSE and Max error.

Among the models with the least RMSE, model derived from Mixed drive cycle test provides better results and reasonable values for core temperature. Although models derived from US06 and Capacity tests have less RMSE and Max error, it is clear from Fig. 5 that their modeled core temperature are not realistic; therefore, these two models cannot be considered as valid models.

Therefore, Mixed drive cycle model with average RMSE of less than 0.5 $°C$ and average Max error of less than 0.8 $°C$ was considered as a valid thermal model. Given this a priori information, Fig. 6 shows the model's validation by using Pulse test and OCV test data. As it was expected core temperature is higher than measured surface temperatures. Since a 10 $°C$ difference between core and surface temperature is recorded for cylindrical batteries [20], 10-13 $°C$ difference in Prismatic batteries is completely realistic [13]. The parameters for this model and the used lower and upper bound can be found in Table 1.

TABLE 1. Thermal model parameters.

Symbol	Unit	Value		
		Identified	LB	UB
C_t	$JºC^{-1}$	203.16	0	2000
C_h	$JºC^{-1}$	113.06	0	2000
C_c	$JºC^{-1}$	3844.3	0	2000
C_b	$JºC^{-1}$	134.78	0	2000
R_1	$ºCW^{-1}$	15.27	0	500
R_2	$ºCW^{-1}$	9.88	0	500
R_3	$ºCW^{-1}$	15.03	0	500
R_4	$ºCW^{-1}$	13.24	0	500
R_5	$ºCW^{-1}$	84.17	0	500
R_6	$ºCW^{-1}$	5.08	3	10
R_7	$ºCW^{-1}$	3.49	3	10
R_8	$ºCW^{-1}$	4.30	3	10

The fluctuation of the battery temperature is because of the cooling flow that tries to keep the temperature at the desired temperature of 25$°C$, which is expected to have the least effect on the core temperature. Based on chamber and battery dimensions and generated heat by battery, for every 1.5 $°C$ rise in battery surface temperature, ambient temperature can rise by 0.8 $°C$. Without the cooling flow of the thermal chamber, the temperature would rise to higher than 55 $°C$, and cause safety concerns [32].

IV. SIMULATION RESULTS

The thermal model for the Prismatic battery is represented as (25) to (32). Using the parameters from Table 1, it is assumed that only the tab temperature is measured during the Pulse test. The measurements from housing and bottom will be used just as a reference to compare the filter's performance. In this section three different filters EKF [33], SVSF [22], 2nd order SVSF [30] are compared with the proposed 3rd order SVSF in terms of accuracy. GA is used

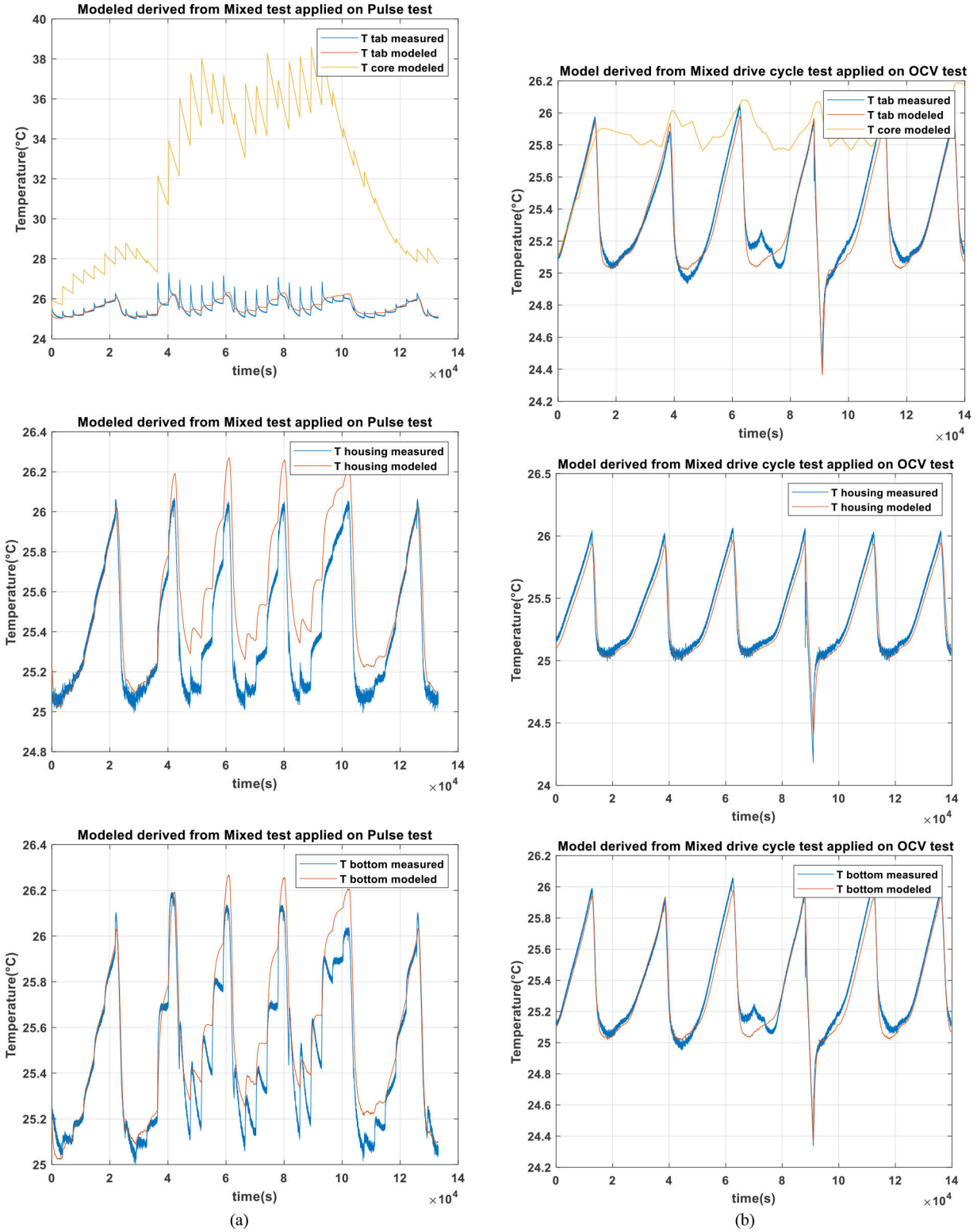

FIGURE 6. Model validation derived from Mixed test on (a) Pulse test (b) OCV test.

to tune the filters as follows:

$$R = 567844,$$
$$Q = diag\,[9051555, 54621, 6180991, 70218]$$
$$P_0 = eye(4) * 14054$$
$$\psi = \begin{bmatrix} 0.098 & 83820.3 & 547008.9 & 644317.1 \end{bmatrix},$$
$$\gamma = 0.0012,\ \Delta T = 1 \tag{33}$$

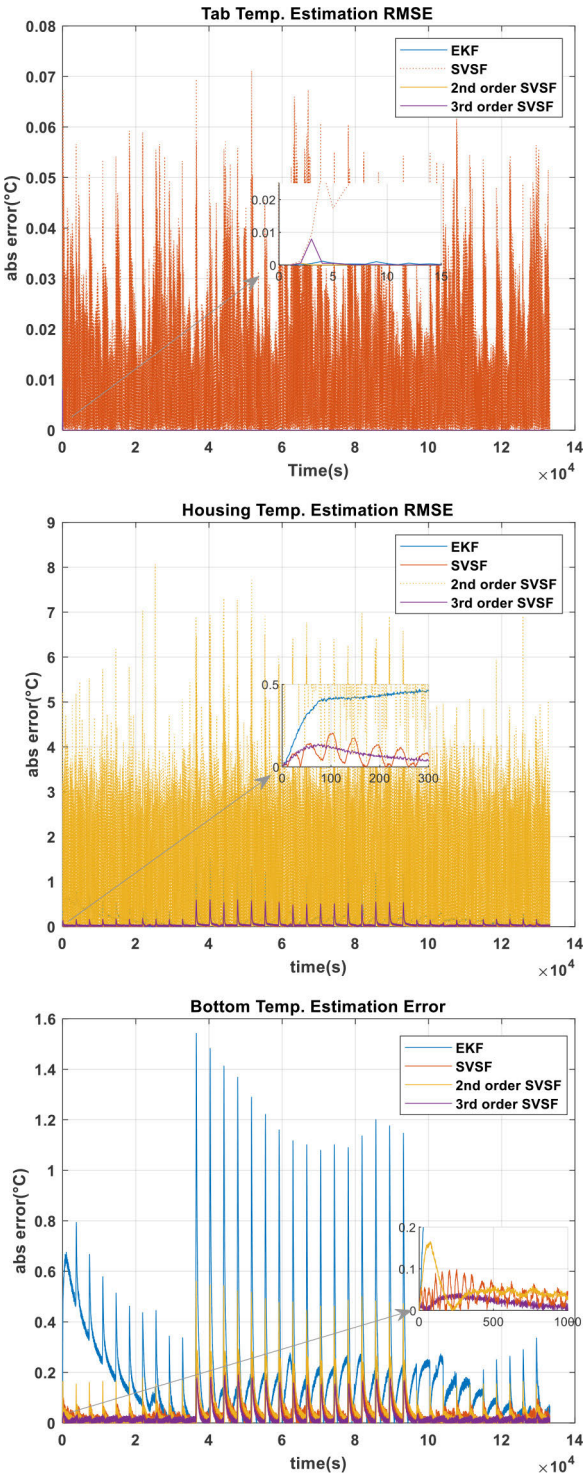

FIGURE 7. Filters' performance for the (a) tab temp. estimation (b) housing temp. estimation (c) bottom temp. estimation.

As shown in Fig. 7., 3rd order SVSF exhibits less chattering and outperforms the other filters by providing less estimation error and lower convergence time. Although the 2nd order SVSF has a better tab temperature estimation, it has difficulty estimating the other surface temperatures. Table 2 summarizes the RMSE and mean RMSE of the four mentioned

TABLE 2. Rmse of the different filters considering $e_{tab,0} = 0°C$.

Filters	Tab RMSE (m°C)	Housing RMSE (m°C)	Bottom RMSE (m°C)	mean RMSE (m°C)
EKF	0.0090	277.9930	273.7507	183.9176
SVSF	15.4298	77.6663	49.0281	47.3747
2nd order SVSF	0.0015	13553	92.2423	482.5210
3rd order SVSF	0.0219	84.2819	38.2980	40.8673

TABLE 3. Rmse of the different filters considering $e_{tab,0} = 2°C$.

Filters	Tab RMSE (m°C)	Housing RMSE (m°C)	Bottom RMSE (m°C)	mean RMSE (m°C)
EKF	5.4905	277.9922	273.7500	185.7442
SVSF	34.0161	252.2270	89.6729	125.3053
2nd order SVSF	5.4810	13553	92.2423	484.3475
3rd order SVSF	5.4810	84.2819	38.2980	42.6870

TABLE 4. Required time to run the algorithms for pulse test.

Filters	EKF	SVSF	2nd Order SVSF	3rd Order SVSF
Means of run time (s)	0.4027	2.1071	1.9372	2.4100

filters. The mean RMSE of the filters proves the superiority of the proposed filter by reducing the RMSE by 77% and 15% compared with that of EKF and SVSF, respectively. For a better comparison and investigation of the robustness of the proposed filter, an initial error of $2°C$ is considered for the tab temperature estimation and the performance of the filters is compared in Table 3. This clearly indicates that the proposed filter is more robust against model uncertainties and initial condition errors than the aforementioned filters.

In order to compare the complexity of the proposed filter with existing filters, 'timeit' operation in MATLAB is used over 150 runs. Table 4 shows mean required time to run different filters. Clearly, 3rd order filter is more complex than SVSF and 2nd order SVSF by 9% and 24%, respectively. Since in this research just one measurement is considered, EKF shows significant difference in terms of complexity, but it goes without saying that with more measurements the inversion operation will increase the complexity of the EKF. As mentioned before, the proposed filter imposes reasonable complexity on the processor while it improves the accuracy substantially.

V. CONCLUSION

In conclusion, this study focused on applying filters to estimate the core, housing, and bottom temperatures of a

Prismatic battery by using only the measured tab temperature. Moreover, a new robust SVSF-based filter is introduced. This filter is named 3rd order SVSF, as it is an extension of SVSF and uses the third derivative of the error. The stability of the filter is proven using a Lyapunov function. The efficiency of the filter was compared with that of the EKF, SVSF, and 2nd order SVSF. Moreover, the experimental part of the battery included a new thermal model of the battery. Unlike the simple model, the four-state model can distinguish between the different points of the battery. The model was derived from a mixed drive cycle test using GA. The heat generated was calculated using the internal resistance of the battery. Therefore, not only is the characterization test used to identify the third-order ECM of the battery, it has also been used to identify the thermal model of the battery.

Our aim as future work is to build an ECM and thermal model over a wide range of temperatures and for different SOHs. These models would enable us to develop a combined ECM/thermal model that can be used for various BMS-oriented projects.

ACKNOWLEDGMENT

The authors would like to thank the invaluable assistance provided by Josimar Duque and Dr. Phil Kollmeyer in conducting the battery characterization tests, and also would like to thank Amirhossein Akbari for his valuable contributions in analyzing the experiments and validating the thermal model.

REFERENCES

[1] S. Rahimifard, "Advanced state estimation for electric vehicle batteries," Ph.D. dissertation, Dept. Mech. Eng., McMaster Univ., Hamilton, ON, CA, 2022.

[2] M. Naguib, "State estimation and thermal fault detection for lithium-ion battery packs: A deep neural network approach," Ph.D. dissertation, Dept. Mech. Eng., McMaster Univ., Hamilton, ON, CA, 2022.

[3] J. G. Zhu, Z. C. Sun, X. Z. Wei, and H. F. Dai, "A new lithium-ion battery internal temperature on-line estimate method based on electrochemical impedance spectroscopy measurement," *J. Power Sources*, vol. 274, pp. 990–1004, Jan. 2015, doi: 10.1016/j.jpowsour.2014.10.182.

[4] L. H. J. Raijmakers, D. L. Danilov, J. P. M. van Lammeren, M. J. G. Lammers, and P. H. L. Notten, "Sensorless battery temperature measurements based on electrochemical impedance spectroscopy," *J. Power Sources*, vol. 247, pp. 539–544, Feb. 2014, doi: 10.1016/j.jpowsour.2013.09.005.

[5] R. R. Richardson, P. T. Ireland, and D. A. Howey, "Battery internal temperature estimation by combined impedance and surface temperature measurement," *J. Power Sources*, vol. 265, pp. 254–261, Nov. 2014, doi: 10.1016/j.jpowsour.2014.04.129.

[6] X. Hu, W. Liu, X. Lin, and Y. Xie, "A comparative study of control-oriented thermal models for cylindrical Li-ion batteries," *IEEE Trans. Transport. Electrific.*, vol. 5, no. 4, pp. 1237–1253, Dec. 2019, doi: 10.1109/TTE.2019.2953606.

[7] J. Lin, X. Liu, S. Li, C. Zhang, and S. Yang, "A review on recent progress, challenges and perspective of battery thermal management system," *Int. J. Heat Mass Transf.*, vol. 167, Mar. 2021, Art. no. 120834, doi: 10.1016/j.ijheatmasstransfer.2020.120834.

[8] X. Hu, W. Liu, X. Lin, Y. Xie, A. M. Foley, and L. Hu, "A control-oriented electrothermal model for pouch-type electric vehicle batteries," *IEEE Trans. Power Electron.*, vol. 36, no. 5, pp. 5530–5544, May 2021, doi: 10.1109/TPEL.2020.3027561.

[9] Y. Xie, X.-J. He, X.-S. Hu, W. Li, Y.-J. Zhang, B. Liu, and Y.-T. Sun, "An improved resistance-based thermal model for a pouch lithium-ion battery considering heat generation of posts," *Appl. Thermal Eng.*, vol. 164, Jan. 2020, Art. no. 114455, doi: 10.1016/j.applthermaleng.2019.114455.

[10] Z. Li, J. Zhang, B. Wu, J. Huang, Z. Nie, Y. Sun, F. An, and N. Wu, "Examining temporal and spatial variations of internal temperature in large-format laminated battery with embedded thermocouples," *J. Power Sources*, vol. 241, pp. 536–553, Nov. 2013, doi: 10.1016/j.jpowsour.2013.04.117.

[11] T. S. Bryden, B. Dimitrov, G. Hilton, C. Ponce de León, P. Bugryniec, S. Brown, D. Cumming, and A. Cruden, "Methodology to determine the heat capacity of lithium-ion cells," *J. Power Sources*, vol. 395, pp. 369–378, Aug. 2018, doi: 10.1016/j.jpowsour.2018.05.084.

[12] M. Akbarzadeh, T. Kalogiannis, J. Jaguemont, J. He, L. Jin, M. Berecibar, and J. Van Mierlo, "Thermal modeling of a high-energy prismatic lithium-ion battery cell and module based on a new thermal characterization methodology," *J. Energy Storage*, vol. 32, Dec. 2020, Art. no. 101707, doi: 10.1016/j.est.2020.101707.

[13] M. Farag, H. Sweity, M. Fleckenstein, and S. Habibi, "Combined electrochemical, heat generation, and thermal model for large prismatic lithium-ion batteries in real-time applications," *J. Power Sources*, vol. 360, pp. 618–633, Aug. 2017, doi: 10.1016/j.jpowsour.2017.06.031.

[14] I. Arasaratnam, J. Tjong, R. Ahmed, M. El-Sayed, and S. Habibi, "Adaptive temperature monitoring for battery thermal management," in *Proc. IEEE Transp. Electrific. Conf. Expo (ITEC)*, Detroit, MI, USA, Jun. 2013, pp. 1–6, doi: 10.1109/ITEC.2013.6574504.

[15] X. Lin, H. E. Perez, J. B. Siegel, A. G. Stefanopoulou, Y. Li, R. D. Anderson, Y. Ding, and M. P. Castanier, "Online parameterization of lumped thermal dynamics in cylindrical lithium ion batteries for core temperature estimation and health monitoring," *IEEE Trans. Control Syst. Technol.*, vol. 21, no. 5, pp. 1745–1755, Sep. 2013, doi: 10.1109/TCST.2012.2217143.

[16] S. Sattarzadeh, T. Roy, and S. Dey, "Real-time estimation of 2-D temperature distribution in lithium-ion pouch cells," *IEEE Trans. Transport. Electrific.*, vol. 7, no. 4, pp. 2249–2259, Dec. 2021, doi: 10.1109/TTE.2021.3071950.

[17] J. M. D. S. Jeewandara, J. P. Karunadasa, and K. T. M. U. Hemapala, "Parametrization and core temperature estimation of lithium-ion batteries for thermal management," in *Proc. IEEE Region Symp. (TENSYMP)*, Aug. 2021, pp. 1–6, doi: 10.1109/TENSYMP52854.2021.9550840.

[18] D. Zhang, L. D. Couto, P. S. Gill, S. Benjamin, W. Zeng, and S. J. Moura, "Thermal-enhanced adaptive interval estimation in battery packs with heterogeneous cells," *IEEE Trans. Control Syst. Technol.*, vol. 30, no. 3, pp. 1102–1115, May 2022, doi: 10.1109/TCST.2021.3091108.

[19] C. Zhang, K. Li, and J. Deng, "Real-time estimation of battery internal temperature based on a simplified thermoelectric model," *J. Power Sources*, vol. 302, pp. 146–154, Jan. 2016, doi: 10.1016/j.jpowsour.2015.10.052.

[20] R. R. Richardson and D. A. Howey, "Sensorless battery internal temperature estimation using a Kalman filter with impedance measurement," *IEEE Trans. Sustain. Energy*, vol. 6, no. 4, pp. 1190–1199, Oct. 2015, doi: 10.1109/TSTE.2015.2420375.

[21] P. Rodríguez-Iturriaga, D. Anseán, J. A. López-Villanueva, M. González, and S. Rodríguez-Bolívar, "A method for the lifetime sensorless estimation of surface and core temperature in lithium-ion batteries via online updating of electrical parameters," *J. Energy Storage*, vol. 58, Feb. 2023, Art. no. 106260, doi: 10.1016/j.est.2022.106260.

[22] S. Habibi, "The smooth variable structure filter," *Proc. IEEE*, vol. 95, no. 5, pp. 1026–1059, May 2007, doi: 10.1109/JPROC.2007.893255.

[23] H. H. Afshari, M. Attari, R. Ahmed, A. Delbari, S. Habibi, and T. Shoa, "Reliable state of charge and state of health estimation using the smooth variable structure filter," *Control Eng. Pract.*, vol. 77, pp. 1–14, Aug. 2018, doi: 10.1016/j.conengprac.2018.04.015.

[24] R. Ahmed, S. Rahimifard, and S. Habibi, "Offline parameter identification and SOC estimation for new and aged electric vehicles batteries," in *Proc. IEEE Transp. Electrific. Conf. Expo (ITEC)*, Detroit, MI, USA, Jun. 2019, pp. 1–6, doi: 10.1109/ITEC.2019.8790474.

[25] T. Kim, A. Adhikaree, R. Pandey, D.-W. Kang, M. Kim, C.-Y. Oh, and J.-W. Baek, "An on-board model-based condition monitoring for lithium-ion batteries," *IEEE Trans. Ind. Appl.*, vol. 55, no. 2, pp. 1835–1843, Mar. 2019, doi: 10.1109/TIA.2018.2881183.

[26] S. Rahimifard, S. Habibi, and J. Tjong, "Dual estimation strategy for new and aged electric vehicles batteries," in *Proc. IEEE Transp. Electrific. Conf. Expo (ITEC)*, Chicago, IL, USA, Jun. 2020, pp. 579–583, doi: 10.1109/ITEC48692.2020.9161556.

[27] S. Rahimifard, R. Ahmed, and S. Habibi, "Interacting multiple model strategy for electric vehicle batteries state of charge/health/power estimation," *IEEE Access*, vol. 9, pp. 109875–109888, 2021, doi: 10.1109/ACCESS.2021.3102607.
[28] M. Messing, S. Rahimifard, T. Shoa, and S. Habibi, "Low temperature, current dependent battery state estimation using interacting multiple model strategy," *IEEE Access*, vol. 9, pp. 99876–99889, 2021, doi: 10.1109/ACCESS.2021.3095938.
[29] A. Wadi, M. F. Abdel-Hafez, A. A. Hussein, and F. Alkhawaja, "Alleviating dynamic model uncertainty effects for improved battery SOC estimation of EVs in highly dynamic environments," *IEEE Trans. Veh. Technol.*, vol. 70, no. 7, pp. 6554–6566, Jul. 2021, doi: 10.1109/TVT.2021.3085006.
[30] H. H. Afshari, S. A. Gadsden, and S. Habibi, "A nonlinear second-order filtering strategy for state estimation of uncertain systems," *Signal Process.*, vol. 155, pp. 182–192, Feb. 2019, doi: 10.1016/j.sigpro.2018.09.036.
[31] M. Nørgaard, N. K. Poulsen, and O. Ravn, "New developments in state estimation for nonlinear systems," *Automatica*, vol. 36, no. 11, pp. 1627–1638, 2000, doi: 10.1016/S0005-1098(00)00089-3.
[32] (May 2018). *LFP Power Battery*. LF280–73103. [Online]. Available: www.dcmax.com.tw/LF280(3.2V280Ah).pdf
[33] Y. Bar-Shalom, X.-R. Li, and T. Kirubarajan, *Estimation With Applications to Tracking and Navigation*. New York, NY, USA: Wiley, 2001, doi: 10.1002/0471221279.

FARZANEH EBRAHIMI received the B.Sc. degree in electrical engineering from Tabriz University, in 2015, and the M.A.Sc. degree in control engineering from Shahid Beheshti University. She is currently pursuing the Ph.D. degree with the Department of Mechanical Engineering, McMaster University. She joined the CMHT Team as part of the battery group working on the battery management system. Her research interests include electric and hybrid technologies, battery management systems, battery modeling, state and parameter estimation, and control theory.

RYAN AHMED received the Ph.D. degree in engineering, focusing on battery modeling, state of charge, and state of health estimation, the Master of Applied Science (M.A.Sc) degree from McMaster, focusing on artificial intelligence and fault detection, and the M.B.A. degree in finance from the DeGroote School of Business. He is currently an Assistant Professor with the Department of Mechanical Engineering, McMaster University. His research interests include smart systems, artificial intelligence, energy storage devices, autonomous systems, and electric powertrains. Prior to joining McMaster, he held several senior engineering positions globally at General Motors, Stellantis, and Samsung. He taught several courses on science, technology, engineering, and mathematics to over more than 340,000 students from 160 countries with more than 29,000 five-star reviews and an overall rating of 4.5/5. He is the principal author and coauthor of over 35 journals and conference publications. He was the co-recipient of two best papers awards at IEEE TRANSACTIONS ON INDUSTRIAL ELECTRONICS, in 2018, and the IEEE Transportation Electrification Conference and Expo (ITEC 2012), Detroit, MI, USA. He is a Stanford Certified Project Manager (SCPM) and a certified Professional Engineer (P.Eng.) in Ontario. He was the Program Co-Chair at the 2017 IEEE Transportation and Electrification Conference (iTEC'17), Chicago, IL, USA.

SAEID HABIBI (Member, IEEE) received the Ph.D. degree in control engineering from the University of Cambridge, U.K. From 2008 to 2013, he was the Chair of the Department of Mechanical Engineering. He is currently a Senior NSERC Industrial Research Chair and a Professor with the Department of Mechanical Engineering, McMaster University, where he is also the Director of the Centre for Mechatronic and Hybrid Technology (CMHT). He has developed his own theory related to estimation referred to as the smooth variable structure filter (SVSF). He has a number of patents and has coauthored close to 200 refereed articles. His academic research interests include intelligent control, state, and parameter estimation, fault diagnosis and prediction, variable structure systems, actuation systems, mechatronics, and fluid power. The application areas for his research have included automotive, aerospace, and robotics. He is a professional engineer and a fellow of ASME and CSME.